Article

Not peer-reviewed version

Manganese Dioxide (MnO_2) Nanoparticles Passivated Perovskite Solar Cell for Improved Power Conversion Efficiency

Simeon Amole , Oluwaseun Adedokun * , Ayodeji Awodugba

Posted Date: 7 May 2024

doi: 10.20944/preprints202405.0334.v1

Keywords: passivation; nanoparticle; enhancement; perovskite; fill factor; counter electrode; organolead

Article

Manganese Dioxide (MnO_2) Nanoparticles Passivated Perovskite Solar Cell for Improved Power Conversion Efficiency

Simeon Amole, Oluwaseun Adedokun * and Ayodeji Awodugba

Lautech; simeonakintola@gmail.com (S.A.); aoawodugba@lautech.edu (A.A.)
* Correspondence: oadedokun@lautech.edu.ng

Abstract: Passivating the grain boundaries is completely very crucial in the enhancement of the performance of halide perovskite solar cells (PSCs). Here, a novel organolead halide perovskite ($CH_3NH_3PbI_3$) was synthesized using solution processes-based method to sensitize 1D titanium dioxide (TiO_2) and reduced graphene oxide (RGO) nanoparticles for all-solid-state halide perovskite solar cells. TiO_2 and RGO were synthesized via sol-gel and Hummers' methods, respectively, and incorporated at the electron transport layer (ETL) in planar PSCs. Additionally, MnO_2 was prepared by chemical method, and used to enhance graphite counter electrode. ITO/RGO/TiO_2/$CH_3NH_3PbI_3$/Gr and ITO/RGO/TiO_2/$CH_3NH_3PbI_3$/Gr-MnO_2 planar PSCs were fabricated via spin coating method. ITO/RGO/TiO_2/$CH_3NH_3PbI_3$/Gr-MnO_2 film achieved a power conversion efficiency (PCE) of 10.79%, short circuit current (Jsc) of 19.0 $mAcm^{-2}$ and fill factor (FF) of 51.53% compared to PCE of 8.64%, Jsc of 16.25 $mAcm^{-2}$ and FF of 47.48% achieved for ITO/RGO/TiO_2/$CH_3NH_3PbI_3$/Gr film. The enhancement value of 22.85% was achieved from J-V curves after exposing the ITO/RGO/TiO_2/$CH_3NH_3PbI_3$/Gr and ITO/RGO/TiO_2/$CH_3NH_3PbI_3$/Gr-MnO_2 films to Keithley 2400 sourcemeter (Keithley Instrument Inc.) under AM 1.5G (100 $mWcm^{-2}$) (Newport) solar illumination in order to test their photovoltaic performance. This study shows that MnO_2 nanoparticle has a proven capability to improve the photovoltaic performance of PSCs.

Keywords: passivation; nanoparticle; enhancement; perovskite; fill factor; counter electrode; organolead

1. Introduction

PSC has a strong possibility for future commercialization owing to its high photoconversion efficiency. The current record for a single-junction perovskite solar cell has now reached 23.7% PCE surpassing the mainstream silicon solar cell. Nonetheless, structural defects such as dangling bonds and vacancies are formed at the GBs due to preparation via solution-based process and crystallization at low temperatures (<100 °C) (Han *et al.*, 2018). Dangling bond provide highways for the migration of ionic and molecular species, and also act as charge recombination centres, leading to recombination, hindering charge mobility and extraction, decreasing photovoltaic performance (Shao *et al.*, 2016). Perovskite films are liable to attack from moisture within GBs, leading to decomposition and poor device stability (Jiang *et al.*, 2016). Because of this, many efforts have been sought to passivate GBs and interfaces to modify the efficiency of PSCs (Yang *et al.*, 2018).

Reports have shown that self-passivation using excess PbI_2 and CH_3NH_3I reduced recombination loss at GBs (Son *et al.*, 2016). But then, these self-passivation methods are sensitive to the preparation conditions, resulting in difficulties associated with reproducibility (Yang *et al.*, 2019). Other studies showed that excess PbI_2 are detrimental to the overall PCE (Tumen-Ulzii *et al.*, 2020). Many other passivation agents have been developed to improve the performance. Organic Lewis acids and bases such as buckminsterfullerene (C_{60}) (Wang *et al.*, 2014), (6,6)-phenyl-C_{61}-butyric acid and methyl ester (PCBM) (Shao *et al.*, 2014) have efficiently reduced the recombination centres in perovskite films leading to increased enhancement in photovoltaic performance. Also, inorganic transition oxide materials such as NiO_x, Cr_2O_4, ZrO_2, Ag and MnO_2 have a proven passivation capabilities owing to their

 doi:10.20944/preprints202405.0334.v1

astonishing structural modularity, straightforward application methods and versatile passivation influences (Gao *et al.*, 2022). MnO_2 has an attractive renewed interest as a promising material owing its high energy density, high theoretical capacitance and completely astonishing structural modularity (Markus *et al.*, 2023). Here, combining graphite and MnO_2 nanoparticle can improve the photovoltaic performance of PSCs

2. Theoretical Consideration

The band gap of perovskite film is calculated by Tauc's plot (Awodugba *et al.*, 2011) which is expressed as:

$$(\propto h\nu)^{\frac{1}{n}} = (h\nu - E_g) \tag{1}$$

$$\alpha = \frac{A}{d} \tag{2}$$

The grain size of the perovskite was calculated using intercept technique, given as (Cheng *et al.*, 2018):

$$g = \frac{b}{a} \tag{3}$$

where a is the number of intersection, and b is the actual length of the line. However, actual length is the ratio of the measured length by the magnification

For the determination of interplanar distance Bragg's law was used

$$n\lambda = 2d\sin\theta \tag{4}$$

Here θ is the one half of peak diffraction angle or Bragg's angle, d is the interplanar distance, λ represents the Cu K(α) wavelength, which in our case is 1.5418 A and n is the mode of vibration.

The crystallite size (L) was determined from the Scherrer equation

$$L = \frac{K\lambda}{\beta\cos\theta} \tag{5}$$

where K is the Scherrer constant (0.9), λ is the wavelength and β is the full width (in radians) of the peak at the half maximum (FWHM) intensity and θ is the one half of peak diffraction angle or Bragg's angle.

Lattice stain (ε) of the materials was calculated by the relation

$$\varepsilon = \frac{\beta\cos\theta}{4} \tag{6}$$

θ is the one half of peak diffraction angle or Bragg's angle and ε is the lattice strain.

The dislocation density δ was calculated using the relation

$$\delta = \frac{1}{L^2} \tag{7}$$

where δ is the dislocation density and L is the crystallite size

The number of reduced graphene oxide layer was calculated using the relation

$$N_{GP} = \frac{L_{002}}{d_{002}} \tag{8}$$

where d_{002} is the d-spacing, N_{GP} is the number of reduced graphene oxide layer and L_{002} is the crystallite size.

To measure the efficiency of a solar cell, the current density of a device is obtained as a function of applied voltage. Such a curve provides the parameters required to calculate efficiency (Walton, Wynne (2018))

$$\eta = \frac{p_{out}}{p_{in}} = \frac{J_{sc}V_{OC}FF}{p_{in}} \tag{9}$$

where η is efficiency, P_{out} is the output power of a device, P_{in} the input power of the incident light, J_{sc} is the short-circuit current density.

 doi:10.20944/preprints202405.0334.v1

V_{oc} is the open-circuit voltage, and FF is a fill factor

$$FF = \frac{J_{mp}V_{mp}}{J_{sc}V_{oc}} \quad (10)$$

where J_{mp}, and V_{mp} are the current density and voltage of the device at its maximum power point, where the value of $J \times V$ is at its maximum in the JV curve. Therefore, to design a high-efficiency solar cell, one may aim to improve the J_{sc}, V_{oc}, or FF.

3. Materials and Methods

3.1. Materials

Lead (II) iodide (PbI_2) 98% purity, titanium isopropoxide ($C_{12}H_{28}O_4Ti$) 96% purity, methyl ammonium iodide (CH_3NH_3I) 98% purity, graphite, potassium per manganese ($KMnO_4$) 96% purity, dimethyl formamide (DMF) 97% purity, isopropanol ($CH_3CH(OH)CH_3$) 99% purity, ethanol (CH_3CH_2OH) 99% purity, hydrochloric acid (HCl) 97% purity, hydrogen tetraoxosulphate (VI) acid (H_2SO_4) 97% purity indium doped tin oxide (ITO) glass and detergent were purchased from commercial suppliers (Fisher Scientific or Sigma-Aldrich).

3.2. Experimental Method

3.2.1. Synthesis of Methyl Ammonium Lead Triiodide ($CH_3NH_3PbI_3$)

Lead (II) iodide (PbI_2) was preheated for 10 minutes at 100 ^oC to evaporate possible humidity within. First, in a process to dissolve PbI_2, 578 mg of it and 200 mg of methyl ammonium iodide (CH_3NH_3I) were mixed with 1 mL of DMF in a test tube and heated 250 ^oC. This temperature was maintained until PbI_2 completely dissolved. The solution was stirred to prevent crystallization of PbI_2. Face mask would be used as safety precaution to prevent the harmful hazard of lead. The perovskite solution was prepared prior to its used because CH_3NH_3I is extremely sensitive to moisture.

$$CH_3NH_3I + PbI_2 \rightarrow CH_3NH_3PbI_3 \quad (11)$$

3.2.2. Synthesis of Titanium Dioxide (TiO_2)Nanoparticles

0.4M of Titanium Isopropoxide was mixed with 1.4M of acetyl acetone and stirred manually for 5 minutes.0.2M of ethanol was then be added to the mixture, and stirred for another 5 minutes. Acetyl acetonate served as stabilizer.

$$C_{12}H_{28}O_4Ti + CH_3CH_2OH \rightarrow Ti(OC_5H_{11})_4 + 4H_2O \rightarrow Ti(OH)_4 + C_5H_{11}OH \text{ (Hydrolysis)}$$
$$Ti(OH)_4 \rightarrow TiO_2 + TiO_2.2H_2O + 2H_2O \text{ (Polymerization)} \quad (12)$$

3.2.3. Synthesis of RGO Nanoparticles

At first, the mixture of 5g of graphite and 15g of potassium per manganese was added slowly to 400mL of 0.5 M hydrogen tetraoxosulphate (VI) acid solution in a three neck flask. The mixture was simultaneously stirred and heated at 50 ^oC for 2 hours using a magnetic stirrer hot plate (modl 78-1). After complete mixing of the solution, 3mL of hydrogen peroxide and 200g of ice was added to the solution to stop the reaction. Thereafter, the mixture was filtered using a filter paper. The residue was then washed with 200mL of distilled water to neutralize the pH and 200mL of 3.2 M hydrochloric acid to remove metal ions. Afterward, 200 mL of ethanol was added to dry the RGO nanoparticles.

 doi:10.20944/preprints202405.0334.v1

3.2.4. Synthesis of MnO_2 Nanoparticles

12 mL of ethanol (CH_3CH_2OH) 99% purity, was added slowly to 12 mL of distilled water in a three neck flask, and the mixture was added to 6 mL of 0.5 M potassium permanganate ($KmnO_4$) solution. The mixture was stirred for 5 minutes using a magnetic stirrer. Thereafter, 3mL of hydrogen peroxide was added as reducing agent and stirred for another 5 minutes to prevent agglomeration. Thereafter, the mixture was filtered using a filter paper. The residue was then washed with 100 mL of ethanol was added to dry the MnO_2 nanoparticles.

3.2.5. Glass/ITO/RGO/TiO_2/$CH_3NH_3I_3$/Graphite- MnO_2 Device Fabrication

The ITO glass slides was cleaned using standard glass cleaning agents in base bath (cleaning agents: deionized water, 1:20), followed by rinsing with deionized water, propanol and ethanol. The glass slides were then dried in an ovum. 2.00 M TiO_2 solution was be prepared in ethanol. One layer of TiO_2 was deposited on the ITO slide glass through spin-coating process (2000 rpm for 30 s) and annealed at 400°C for 1 hr.1.00 M of RGO was prepared in ethanol. One layer of TiO_2 was spin-coated at 2000 rpm for 30 s and annealed at 400°C for 1 hr. A solution of 578 mg of PbI_2 and 200 mg of CH_3NH_3I in 1 mL of DMF was prepared, heated at 250°C, and deposited via spin coating steps (2000 rpm for 20 s, 2000 rpm for 10 s). The $CH_3NH_3I_3$ was allowed to dry for 1 hr. 1.00 M of MnO_2 was prepared in ethanol and 1mL of it was mixed with 5 mL of a solution of 0.006g graphite in 0.04g of ethanol. Afterward enhanced graphite was deposited by spin coating (2000 rpm for 30 s).

3.2.6. Glass/ITO/RGO/TiO_2/$CH_3NH_3I_3$/Graphite Device Fabrication

The ITO glass slides was cleaned using standard glass cleaning agents in base bath (cleaning agents: deionized water, 1:20), followed by rinsing with deionized water, propanol and ethanol. The glass slides were then dried in an ovum. 2.00 M TiO_2 solution was be prepared in ethanol. One layer of TiO_2 was deposited on the ITO slide glass through spin-coating process (2000 rpm for 30 s) and annealed at 400°C for 1 hr.1.00 M of RGO was prepared in ethanol. One layer of TiO_2 was spin-coated at 2000 rpm for 30 s and annealed at 400°C for 1 hr. A solution of 578 mg of PbI_2 and 200 mg of CH_3NH_3I in 1 mL of DMF was prepared, heated at 250°C, and deposited via spin coating steps (2000 rpm for 20 s, 2000 rpm for 10 s). The $CH_3NH_3I_3$ was allowed to dry for 1 hr. Afterward enhanced graphite was deposited by spin coating (2000 rpm for 30 s) from a solution of 0.006g graphite in 0.04g of ethanol.

3.3. Characterization of the Films

The Ultraviolet-visible spectrophotometer (Lambda 950) was used to study the optical properties such as intensity and wavelength of the absorption spectral of the formed films. X-ray diffraction patterns were obtained with Rigaku D/Max-lllC X-ray diffractometer developed by the Rigaku Int. Corp. Tokyo, Japan, and set to produce diffractions at scanning rate of 2°/min in the 2 to 50° at room temperature with a CuKa radiation set at 40kV and 20mA. Scanning electron microscopy (SEM) images were acquired using a JEOL JSM-6010LV microscope at an accelerating voltage of 15 KV, and a working distance of 11 mm. All spectra were recorded from 4000 to 400 cm-1 using the Pelkin Elmer 3000 MX spectrometer. Scans were 32 per spectrum with a resolution of 4 cm^1.The IR spectra were analysed using the spectroscopic software Win-IR Pro Version 3.0 with a peak sensitivity of 2 cm^{-1}.

4. Results

4.1.1. Optical Characterization of $CH_3NH_3PbI_3$

Figure 1a shows absorbance-wavelength plot of $CH_3NH_3PbI_3$ with its distinct absorption edges. It is clear that the absorption onset systemically located at 652 nm. Besides, the graph reveals another absorbance peaks corresponding to 722 nm. This shows that $CH_3NH_3PbI_3$ absorbs within the visible region with longer wavelength range of between 395-800 nm. Transmittance-wavelength plot in

 doi:10.20944/preprints202405.0334.v1

Figure 1b clearly shows the transmittance onset at 485 nm. The plot shows gradual increase in transmittance between the wavelength range of 485 nm -650 nm, and transmits steadily within the visible region of solar spectrum with longer wavelength range between 500 - 800 nm. The bandgap of the synthesized $CH_3NH_3PbI_3$ film in Figure 1c is 1.67 eV. The bandgap value of 1.67 eV for perovskite is within the acceptable range 1.6 - 1.9 eV (Masclocene et al., 2021)

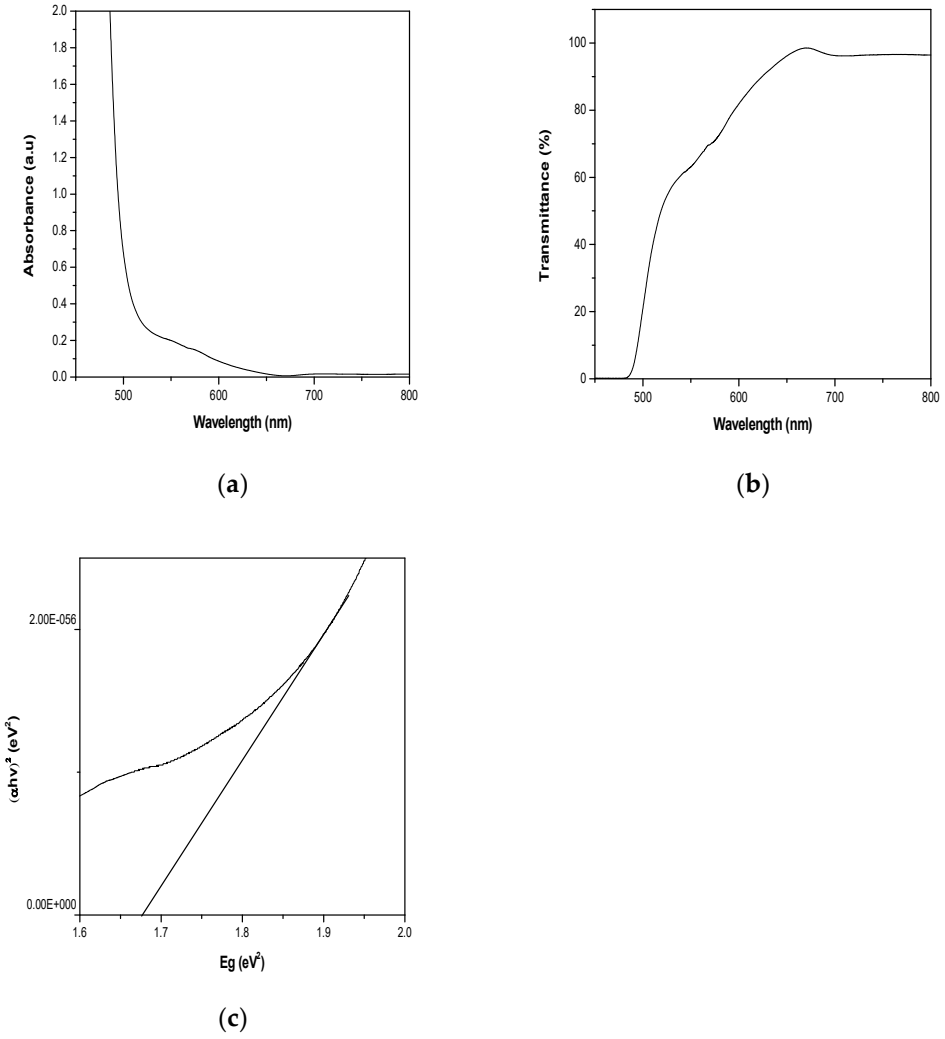

Figure 1. (**a**)Absorbance-wavelength plot of $CH_3NH_3PbI_3$ (**b**) Transmittance-wavelength plot of $CH_3NH_3PbI_3$ (c) $(\alpha hv)^2$-Eg plots of $CH_3NH_3PbI_3$.

4.1.2. FTIR Characterization of $CH_3NH_3PbI_3$ Film

Several molecular vibration frequencies are identified which include $CH_3NH_3^+$ ($V_{CH_3NH_3^+}$,1029.00 cm^{-1}), C=N ($V_{C=N}$, 1742.77 cm^{-1}), C-C (V_{C-C}, 726.26 cm^{-1}), C-H (V_{C-H}, 2924.00 and 2857.00 cm^{-1}), C-O-C (V_{C-O-C}, 1165.00 cm^{-1}), NH_2 (V_{NH2}, 3305.00 cm^{-1}) and O-H (V_{C-OH},3455.00 cm^{-1}). These functional groups are in keeping with cubic phase of $CH_3NH_3PbI_3$ halide perovskite.

Table 1. Summary of bondtypes and wavenumbers in $CH_3NH_3PbI_3$ FTIR spectrum.

Peak	Wave number (cm^{-1})	Bond type
1	3450.00	OH stretch
2	3305.00	$\mathbf{CH_3NH_3^+}$ stretch

Preprints.org (www.preprints.org) | NOT PEER-REVIEWED | Posted: 7 May 2024 doi:10.20944/preprints202405.0334.v1

3	2925.00	CH_3 bend
4	2860.00	CH_2 bend
5	1742.77	C=N stretch
6	1165.00	C-O-C stretch
7	1065.00	NH_2 scissor
8	725.00	C-H stretch
9	629.00	C-I stretch

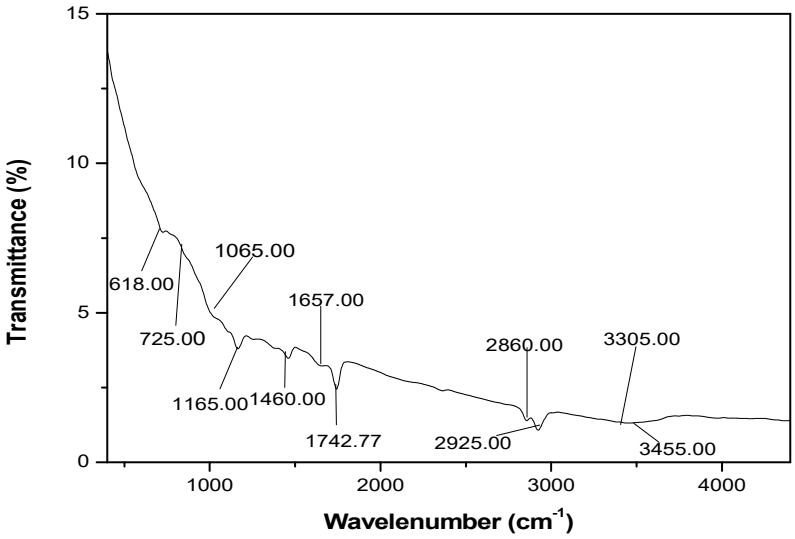

Figure 2. FTIR spectra of $CH_3NH_3PbI_3$ film showing bond type and wavenumber.

4.1.3. XRD Characterization of $CH_3NH_3PbI_3$ Halide Perovskite Film

XRD measurements were performed and results are shown in Figure 3. The most prominent perovskite peak is at the (101) reflection, observed at 2θ =28.8° compatible with a single- crystalline phase. Three other strong diffraction peaks are located at 32.0°, 45.4° and 56.1° corresponding to the (100), (200) and (220) crystal planes of cubic phase $CH_3NH_3PbI_3$ halide perovskite respectively. Additionally, the presence of peaks at 28.8° and 45.4° indicates presence of CH_3NH_3I crystallization in perovskite films, supporting the conversion of the precursor materials into $CH_3NH_3PbI_3$ films, and the appearance of the diffraction angles 28.8°.confirmed cubic phase $CH_3NH_3PbI_3$ halide perovskite. From the data in Table 2, the average crystallite size and d-spacing were calculated to be ~ 7.86 nm and ~ 1.79 Å respectively.

Table 2. Structural parameters of in $CH_3NH_3PbI_3$ film.

Peak	2θ (°)	FWHM (°)	Count (a.u)	d (Å)	hkl	L (nm)	ε (%)	δ (nm^{-2})
1	28.8	1.028	2500	3.096	101	8.34	0.248	0.0143
2	34.0	1.130	1000	2.633	100	7.68	0.270	0.0169
3	40.2	1.143	1000	1.080	200	7.74	0.268	0.0166
4	49.9	1.130	800	1.825	220	8.10	0.256	0.0152

Preprints.org (www.preprints.org) | NOT PEER-REVIEWED | Posted: 7 May 2024 doi:10.20944/preprints202405.0334.v1

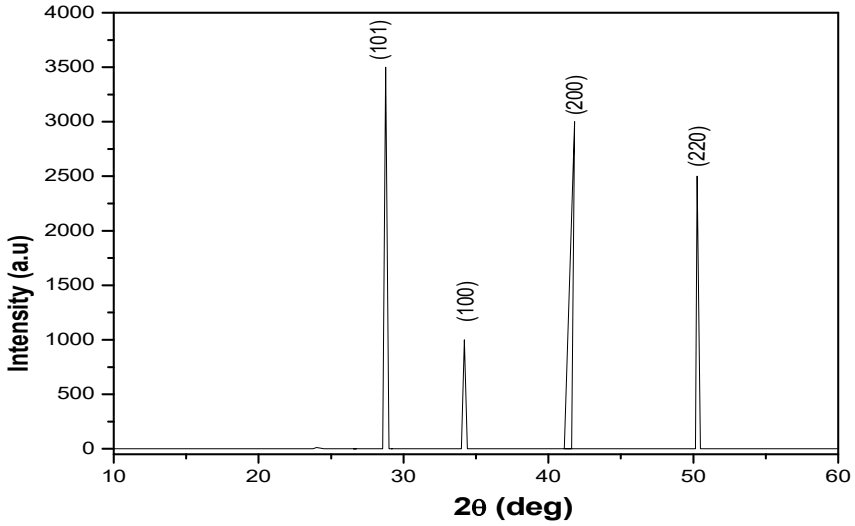

Figure 3. XRD pattern of $CH_3NH_3PbI_3$ film.

4.1.4. SEM Analysis of $CH_3NH_3PbI_3$ Film

Figure 4 a,b show the SEM images of $CH_3NH_3PbI_3$ film at 7000 and 8000 magnifications. The Figure 4 shows high film coverage, compact structure, uniform morphology and smooth surface with apparent grain boundries typical of $CH_3NH_3PbI_3$ films prepared by solution process in one step. No cracks were observed. In perovskite films, the smoothness of each layer is crucial for interface contact. The smooth surface of perovskite thin films lead to the reduced interface resistance of the perovskite, and reduce charge recombination loss at the interface of perovskites. It was reported that the smoothness of perovskite film is necessary to obtain high quality interfaces and high photoconversion efficiency.

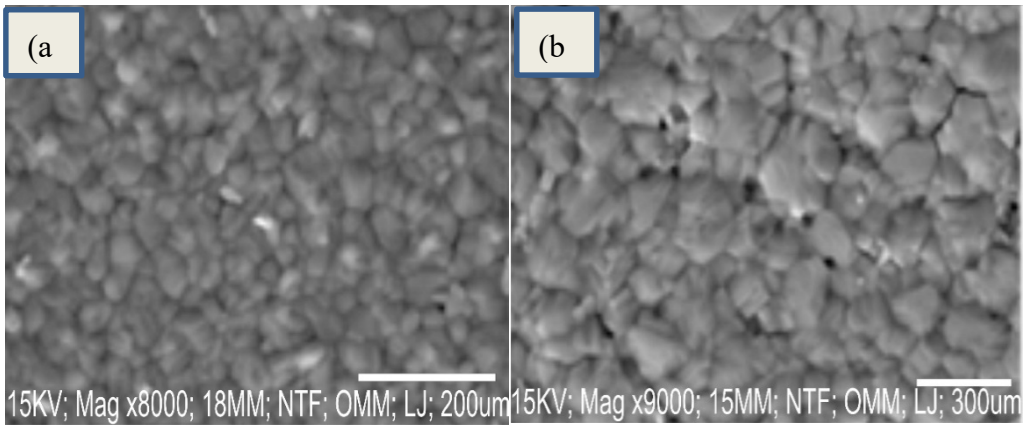

Figure 4. SEM images of $CH_3NH_3PbI_3$ film.

4.2.1. FTIR Characterization of TiO_2, RGO and MnO_2 Nanoparticles

As seen in Figure 4a, several molecular vibration frequencies are identified which include OH (V_{OH}3380.00 cm^{-1},1619.00 cm^{-1}), C-H (V_{C-H}, 2355.00 cm^{-1}) and Ti-O-Ti ($V_{Ti-O-Ti}$, 560.00 cm^{-1}, 460.00 cm^{-1}). As see Figure 4b, the hydroxyl compound functional group (–OH) formed at the peak with a wavenumber of 3438.51 cm^{-1}, the aromatic carbon functional group (C=C) formed at the peak with a wavenumber of 1665.02 cm^{-1}, and the epoxy functional group (–CO) formed at the peak with a wavenumber of 1216.14 cm^{-1}. Additionally, alkoxy functional group(–C–O) is located at the peak with a

 doi:10.20944/preprints202405.0334.v1

wavenumber 1028.88 cm $^{-1}$ and the absorption peak with a wavenumber of 2886.00 cm^{-1} signifying the existence –C-H stretching mode (Konios *et al.*, 2014). Figure 4c represents the FTIR spectrum of MnO_2 nanoparticles. Two broad bands appear at 3400.00 cm^{-1} and 1650.00 cm^{-1}. Both bands are the characteristic and specific bands for O–H group representing stretching and bending vibration respectively for surface-adsorbed hydroxyl groups in water (Suriyavathana *et al.*, 2015). The absorption peak with a wavenumber of 2886.00 cm^{-1} signifying the existence –C-H stretching mode (Konios *et al.*, 2014). Besides, the transmission peaks 765.00 cm^{-1} and 528.00 cm^{-1} represent the stretching vibration of Mn-O bonds, and characteristic stretching of O–Mn–O.

Table 3. Summary of bond types and wavenumber in TiO_2, RGO and MnO_2.

Peak	Wave number (cm^{-1})			Bond type
	TiO_2	RGO	MnO_2	
1	3380.00	3438.51	3400.02	O-H stretch
2	—	2886.00	2860.00	C-H stretch
3	2355.00	—	—	C-H stretch
4	—	1665.02	—	C=H stretch
5	—	—	1650.00	O-H bend
6	—	1216.14	—	C-O stretch
7	—	1028.88	—	C-O stretch
8	—	—	765.00	Mn-O stretch
9	560.00	—	—	Ti-O-Ti stretch
10	—	—	528.00	Mn-O stretch
11	460.00	—	—	Ti-O-Ti bend

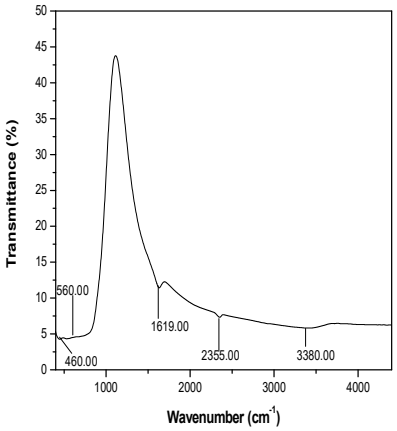

(**a**)

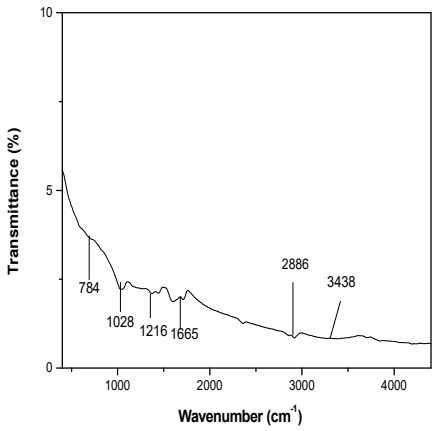

(**b**)

 doi:10.20944/preprints202405.0334.v1

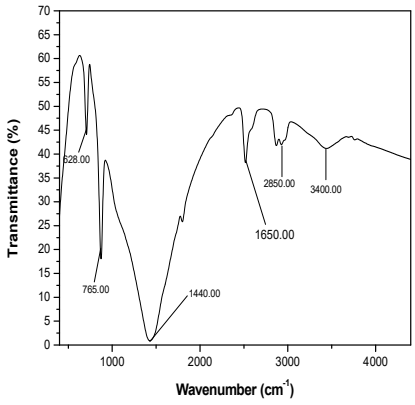

(**c**)

Figure 4. (a)FTIR spectrum of TiO_2 nanoparticles (b)FTIR spectrum of RGO nanoparticles(a)FTIRspectrum of MnO_2 nanoparticles.

4.2.2. XRD Characterization of TiO_2, RGO and MnO_2 Nanoparticles

Figure 5a shows the TiO_2 film XRD patterns. The presence of a sharp peak which corresponds to plane(110) at 2θ = 27.59° referring to the rutile phase having tetragonal structure. The diffraction peaks for planes (001), (201), (101), (110), (101), (111) and (211) at 2θ=7.60°, 2θ=14.89°, 2θ=29.75°, 2θ=27.50°, 2θ=37.10°, 2θ=42.50° and 2θ= 54.60° reflect the tetragonal structure of TiO_2 nanoparticles. As seen in Table 4, the average crystallite size of 59.78 nm, lattice strain of 0.032 % and dislocation density of 0.00030 nm^{-2} were also calculated. The diffraction patterns for MnO_2 are given in Figure 5b. The presence of diffraction peaks for planes (110), (200), (310), (311) and (410) at 2θ=18.27°, 2θ=24.80° and 2θ=28.75°, 2θ=42.50° and 51.20° reveal the alpha phase having pattern of tetragonal structure conformity with (JCPDS Card No.44-0141) having the lattice constants of (a = b = 9.78475 Å, c = 2.86302 Å) and ($\alpha = \beta = \gamma = 90°$). As seen in Table 5, the average crystallite size of 53.87 nm, lattice strain of 0.040 % and dislocation density of 0.00039 nm^{-2} were also calculated. The XRD pattern of the synthesized RGO as shown in Figure 6 demonstrated peaks at 2θ=22.10° and 2θ =28.20° which is the characteristics of carbonaceous material. The most prominent peak located at 2θ=22.10° and other strong diffraction peak at 2θ=22.10° correspond to (002) and (200) basal planes respectively. Additionally, the d-spacing of film decreases as the diffraction tends towards larger angle with average d-spacing value of ~ 4.095 Å compared to ~ 7.37 Å obtained for graphene oxide by Mohamed et al, 2015.

Table 4. Structural parameters of TiO_2 film.

Peak	2θ (°)	FWHM (°)	Count (a.u)	d (Å)	hkl	L (nm)	ε (%)	δ (nm^{-2})
1	13.6	0.118	800	6.503	001	70.84	0.029	0.000199
2	16.9	0.120	600	5. 240	201	60.93	0.029	0.000269
3	24.8	0.139	100	3.585	101	61.14	0.033	0.000267
4	27.5	0.134	1300	3.229	110	63.79	0.013	0.000170
5	36.2	0.120	800	2.478	101	72.77	0.028	0.000188
6	42.2	0.192	400	2.138	111	46.34	0.044	0.000465
7	54.8	0.228	200	1.693	211	42.50	0.050	0.000553

 doi:10.20944/preprints202405.0334.v1

Table 5. Structural parameters of RGO film.

Peak	2θ (˚)	FWHM (˚)	Count (a.u)	d (Å)	hkl	L (nm)	ε (%)	δ (nm^{-2})	N_{GP}
1	22.1	0.181	550	4.881	100	46.44	0.044	0.000463	9.51
2	28.8	0.121	900	3.309	310	70.83	0.029	0.000199	21.40

Table 6. Structural parameters of MnO_2 film.

Peak	2θ (˚)	FWHM (º)	Count (a.u)	d (Å)	hkl	L (nm)	ε (%)	δ (nm^{-2})
1	18.1	0.181	550	4.881	100	46.44	0.044	0.000463
2	28.8	0.121	900	3.309	310	70.83	0.029	0.000199
3	37.5	0.134	750	2.391	211	65.43	0.031	0.000233
4	40.6	0.192	1100	2.119	310	46.40	0.045	0.000464
5	50.5	0.228	400	1.805	411	40.25	0.051	0.000617

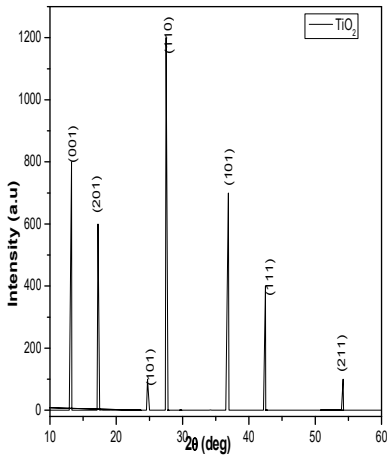

(a)

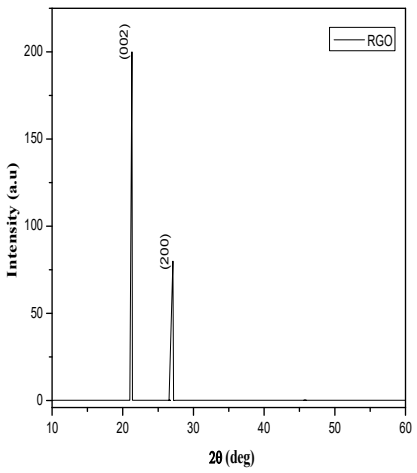

(b)

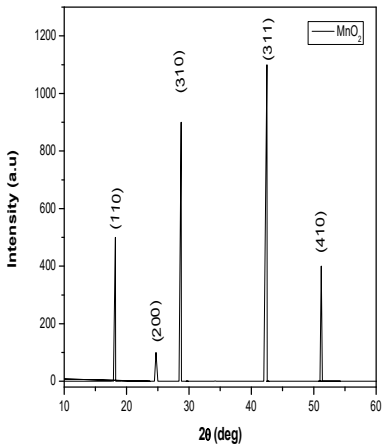

(c)

Figure 5. (a) XRD pattern of TiO_2 nanoparticles (b) XRD pattern of RGO nanoparticles (c) XRD pattern of MnO_2 nanoparticles.

 doi:10.20944/preprints202405.0334.v1

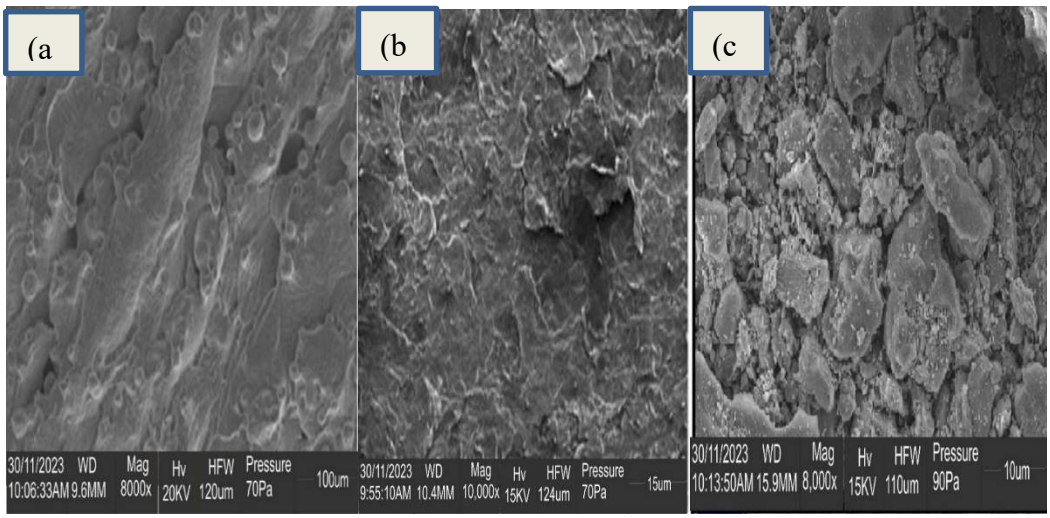

Figure 6. (a) SEM image of TiO_2 nanoparticles (b) SEM image of RGO nanoparticles (c) SEM image of MnO_2 nanoparticles.

4.2.3. SEM Characterization of TiO_2, RGO and MnO_2 Nanoparticles

The SEM image of TiO_2 in Figure 6a demonstrated properly-aligned structures of oval shapes constructed by nearly homogenous grains. Additionally, the surface was smooth and presents the crystalline nature of the produced film. SEM image of RGO is shown in Figure 6b. The morphology of multilayer RGOs revealed rough surface, flake-like shape, not crumpled and corrugated together with non-uniform of particle size. High film coverage was also observed. The aggregation or coalescence of flakes were large and ubiquitous. The agglomeration of the flakes was owing to catalytic oxidation of graphite by surphuric acid (Bhatti *et al.*, 2016). As seen in Figure 6c, the morphology study results of MnO_2 nanoparticle film exhibit high-quality nanocomposites having different micrometers average length. The particle size was elongated and nearly spherical.

3.3.1. Optical Characterization of ITO/RGO/ TiO_2/$CH_3NH_3PbI_3$/Gr and ITO/RGO/ TiO_2/$CH_3NH_3PbI_3$/Gr- MnO_2 Films

Figure 7a shows the UV-vis absorption spectra of the ITO/RGO/TiO_2/$CH_3NH_3PbI_3$/Gr and ITO/RGO/TiO_2/$CH_3NH_3PbI_3$/Gr-MnO_2 films. the modification showed increases the intensity of absorption (hyperchromic effect) due to the increase in the number of delocalized electrons leading to a quasi-fermi level. This high absorbance intensity is attributed to the presence of simple un-conjugated chromophore with lone pair electrons in the MnO_2 and ITO/RGO/TiO_2/$CH_3NH_3PbI_3$/Gr. As a result, there was a high energy transition from an occupied molecular orbital (a non-bonding π orbital) to an unoccupied molecular orbital (σ^* orbital) of greater potential energy. i.e., $\pi \rightarrow \sigma^*$ (Subodh, 2006). The $(\alpha hv)^2$-Eg plots of ITO/RGO/TiO_2/$CH_3NH_3PbI_3$/Gr and ITO/RGO/TiO_2/$CH_3NH_3PbI_3$/Gr-MnO_2 film is shown in Figure 7b. The band gap of fabricated ITO/RGO/TiO_2/$CH_3NH_3PbI_3$/Gr solar cell was extrapolated to be 1.75 eV, and that of ITO/RGO/TiO_2/$CH_3NH_3PbI_3$/Gr-MnO_2 reduced to 1.66 eV.

 doi:10.20944/preprints202405.0334.v1

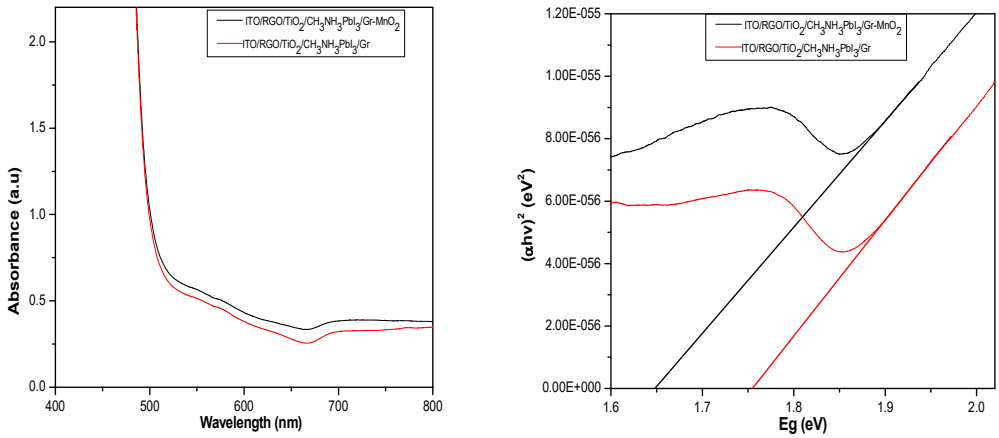

Figure 7. (a) Absorbance-wavelength plots of ITO/RGO/ TiO_2/$CH_3NH_3PbI_3$/Gr and ITO/RGO/ TiO_2/$CH_3NH_3PbI_3$/Gr- MnO_2 films (b) $(\alpha hv)^2$-Eg plots of ITO/RGO/ TiO_2/$CH_3NH_3PbI_3$/Gr and ITO/RGO/ TiO_2/$CH_3NH_3PbI_3$/Gr- MnO_2 films.

4.3.2. FTIR Characterization of ITO/RGO/ TiO_2/$CH_3NH_3PbI_3$/Gr and ITO/RGO/ TiO_2/$CH_3NH_3PbI_3$/Gr- MnO_2 Films

FTIR analysis was carried out to investigate the interaction between MnO_2 and ITO/RGO/TiO_2/$CH_3NH_3PbI_3$/Gr and results shown in Figure 8. In the fingerprint region of MnO_2 FTIR spectrum, two absorption peaks 528.00 cm^{-1} and 765.00 cm^{-1} which could be assigned to Mn-O-Mn and Mn-O. These two peaks present in ITO/RGO/TiO_2/$CH_3NH_3PbI_3$/Gr FTIR spectrum which confirmed incorporation of MnO_2 within the ITO/RGO/TiO_2/$CH_3NH_3PbI_3$/Gr specie. The peaks of Mn-O-Mn and Mn-O were located at 528.00 cm^{-1} and 765.00 cm^{-1} in MnO_2 film, while these peaks red shift to 556.00 cm^{-1} and 825.00 cm^{-1}. Besides, the asymmetric NH_3^+ bend, symmetric NH_3^+ bend and CH_3 NH_3^+ stretch located at 2886.00 cm^{-1}, 1445.00 cm^{-1} and 976.00 cm^{-1} in ITO/RGO/TiO_2/$CH_3NH_3PbI_3$/Gr film blue shift to 2880.00 cm^{-1}, 1442.00 cm^{-1} and 975.00 cm^{-1}. The blue shift of ITO/RGO/TiO_2/$CH_3NH_3PbI_3$/Gr film peak and red shift of MnO_2 peak confirmed that there was strong coordination interaction between the functional groups of MnO_2 and Pb defects of the grain boundaries and interfaces of ITO/RGO/TiO_2/$CH_3NH_3PbI_3$/Gr film.

Table 7. Summary of bond types and wavenumber in MnO_2, ITO/RGO/TiO_2/$MAPbI_3$/Gr and ITO/RGO/TiO_2/$MAPbI_3$/Gr.

Peak	Wave number (cm^{-1})			Bond type
	MnO_2	ITO/RGO/TiO_2/$MAPbI_3$/Gr	ITO/RGO/TiO_2/$MAPbI_3$/Gr	
1	3400.00	3420.00	3602.00	OH stretch
2	—	2886.00	2880.00	NH_3^+ bend
3	2850.00	—	2890.00	C-H stretch
4	—	1445.00	1442.00	NH_3^+ bend
5	—	976.00	975.00	$CH_3NH_3^+$ stretch
6	1668.00	—	1920.00	OH bend
7	1445.00	—	1116.00	C_6H_6 ring
8	765.00	—	825.00	Mn-O
9	528.00	—	556.00	Mn-O-Mn

 doi:10.20944/preprints202405.0334.v1

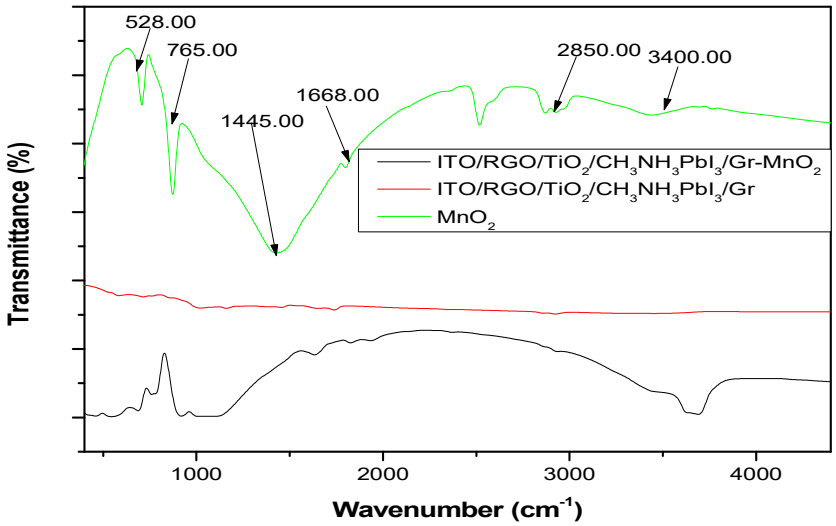

Figure 8. FTIR spectrum of MnO_2, ITO/RGO/TiO_2/MAPbI$_3$/Gr and ITO/RGO/TiO_2/MAPbI$_3$/Gr.

3.3.3. XRD Characterization of ITO/RGO/ TiO_2/$CH_3NH_3PbI_3$/Gr and ITO/RGO/ TiO_2/$CH_3NH_3PbI_3$/Gr- MnO_2 Films

In order to investigate the effect of MnO_2 on the crystallinity of ITO/RGO/TiO_2/$CH_3NH_3PbI_3Br$/Gr film. XRD measurements were performed and the results are shown in Figure 9. Five XRD peaks at 2θ= 19.20°, 27.90°, 29.80°, 38.90° and 59.20° were observed in the two perovskite films which correspond to (101), (111), (210), (200) and (310) crystal plane of cubic phase $CH_3NH_3PbI_3$halide perovskite. The XRD results confirmed that MnO_2 has no remarkable influence on the crystal phase of ITO/RGO/TiO_2/$CH_3NH_3PbI_3$/Gr film by the addition of MnO_2 (Xu *et al.*, 2018). The intensities of 19.20°, 27.90°, 38.90° and 59.20° XRD peaks of ITO/RGO/TiO_2/$CH_3NH_3PbI_3$/Gr-MnO_2 film were higher than those of ITO/RGO/TiO_2/$CH_3NH_3PbI_3$/Gr film, and the narrowed widths of these diffraction angles indicating that MnO_2 incorporation enhanced the crystallinity of ITO/RGO/TiO_2/$CH_3NH_3PbI_3$/Gr film consistent with reports of other additives used in perovskites (Chavan *et al.*, 2020).

Table 8. Summary of structural parameter MnO_2, ITO/RGO/TiO_2/MAPbI$_3$/Gr and ITO/RGO/TiO_2/MAPbI$_3$/Gr.

2θ (˚)	2θ (˚)	β_1 (˚)	β_2 (˚)	d_1 (Å)	d_2 (Å)	L_1 (nm)	L_2 (nm)	ε_1 (%)	ε_2 (%)	δ_1 (nm^{-2})	δ_2 (nm^{-2})
18.95	19.20	0.011	0.010	9.355	9.234	765.04	841.25	0.0023	0.0025	1.7X10^{-6}	1.4X10^{-6}
27.25	27.90	0.021	0.018	6.537	6.388	406.72	475.00	0.0040	0.0046	6.0X10^{-6}	4.4X10^{-6}
29.50	29.80	0.012	0.012	6.048	5.989	715.30	715.30	0.0026	0.0026	1.9X10^{-6}	1.9X10^{-6}
38.20	38.90	0.017	0.011	4.706	4.624	516.73	800.30	0.0021	0.0033	3.7 X10^{-6}	3.7X10^{-6}
58.80	59.20	0.020	0.021	3.137	3.137	476.43	454.61	0.0027	0.0025	4.4 X10^{-6}	4.8X10^{-6}

 doi:10.20944/preprints202405.0334.v1

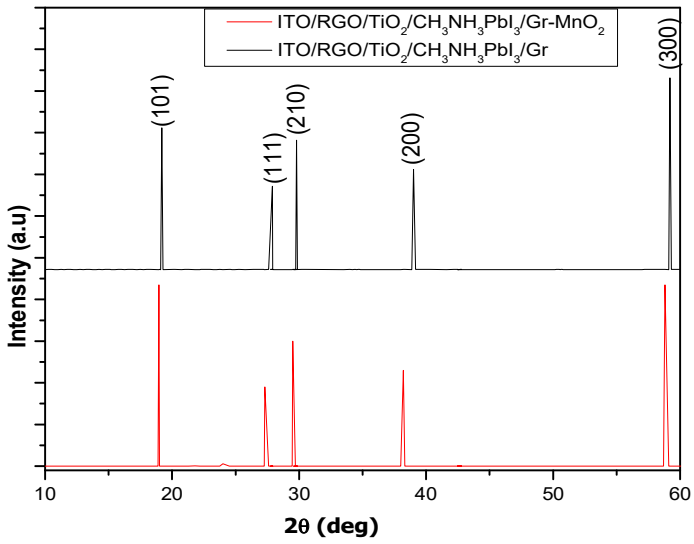

Figure 9. XRD patterns of ITO/RGO/ TiO_2/CH $_3NH_3PbI_3$/Gr and ITO/RGO/ TiO_2/$CH_3NH_3PbI_3$/Gr-MnO_2 films.

4.3.4. SEM Characterization of ITO/RGO/ TiO_2/CH $_3NH_3PbI_3$/Gr and ITO/RGO/ TiO_2/$CH_3NH_3PbI_3$/Gr-MnO_2 Films

The reference film without MnO_2 showed high film coverage, uniform morphology with apparent grain boundaries (Figure 9a) typical of perovskite films synthesized using the solution processed in one step method (Yang *et al.*, 2019, He *et al.*, 2020, Chiang *et al.*, 2017). There was an evidence of compositional uniformity, and thus the grain boundaries were ubiquitous. No cracks were observed throughout the films (Figure 10a).Interesting, ITO/RGO/TiO_2/$CH_3NH_3PbI_3$/Gr film modified with MnO_2 exhibited a more uniform and compact structure compared to the reference film (Figure 9b). As seen in Figure 9b, there was evidence of more smooth surface which confirmed crystallinity enhancement. The average grain size(s) calculated for ITO/RGO/TiO_2/$CH_3NH_3PbI_3$/Gr and ITO/RGO/TiO_2/$CH_3NH_3PbI_3$/Gr-MnO_2 films were ~ 620 nm and ~ 696 nm using intercept technique. This result confirms the morphology improvement of ITO/RGO/TiO_2/$CH_3NH_3PbI_3$/Gr modified with MnO_2.

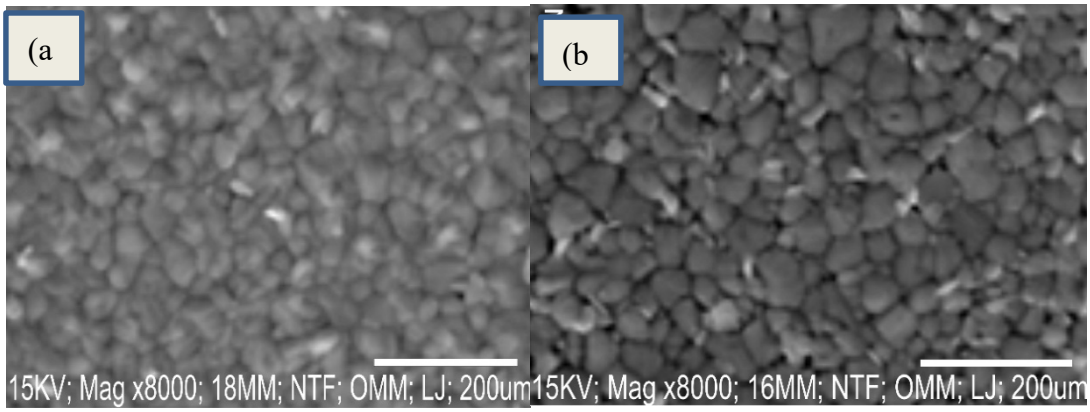

Figure 10. SEM images of ITO/RGO/ TiO_2/CH $_3NH_3PbI_3$/Gr and ITO/RGO/ TiO_2/$CH_3NH_3PbI_3$/Gr-MnO_2 films.

 doi:10.20944/preprints202405.0334.v1

4.3.5. Photovoltaic Performance of ITO/RGO/ TiO_2/$CH_3NH_3PbI_3$/Gr and ITO/RGO/ TiO_2/$CH_3NH_3PbI_3$/Gr- MnO_2 Films

The photovoltaic performance parameters (such as Jsc, Voc, FF, and PCE) are shown in the Figure 11 As seen in Table 9, the incorporation of MnO_2 into the second device produced an increased in the value of Jsc from 16.25 $mAcm^{-2}$ to 19.00 $mAcm^{-2}$. This is due to the improved charge extraction and transfer ability induced in the second device by modification with MnO_2.nanoparticles. FF also increased from 47.48 % to 51.53 %. This indicates that the incorporation of MnO_2 enhanced the grain size of the perovskite absorber and the crystallinity of the absorber at the interface between the absorber and the ETL. As the grain size increases, the grain boundary reduces, thereby eliminating the charge trapping regions within the perovskite structure. However, the variation in the values of Voc in both devices could be as a result of hysteresis effect (Ihly et al, 2016). From the obtained photovoltaic parameters, the PCE increased from 8.64% to 10.79% with an enhancement value of 21.79%. This is due to tailored functionality of MnO_2 in the generation of functional group that act as conducting bridge in reducing the contact resistance between individual nanoparticle.

Table 9. Summary of Photovoltaic parameter of ITO/RGO/TiO_2/$MAPbI_3$/Gr and ITO/RGO/TiO_2/$MAPbI_3$/Gr.

Device	Archetecture	Jsc ($mAcm^{-2}$)	Voc (V)	FF (%)	PCE (%)
1	ITO/RGO/TiO_2/$CH_3NH_3PbI_3$/Gr	19.00	1.20	47.48	8.64
2	ITO/RGO/TiO_2/$CH_3NH_3PbI_3$/Gr-MnO_2	16.25	1.10	51.53	10.79

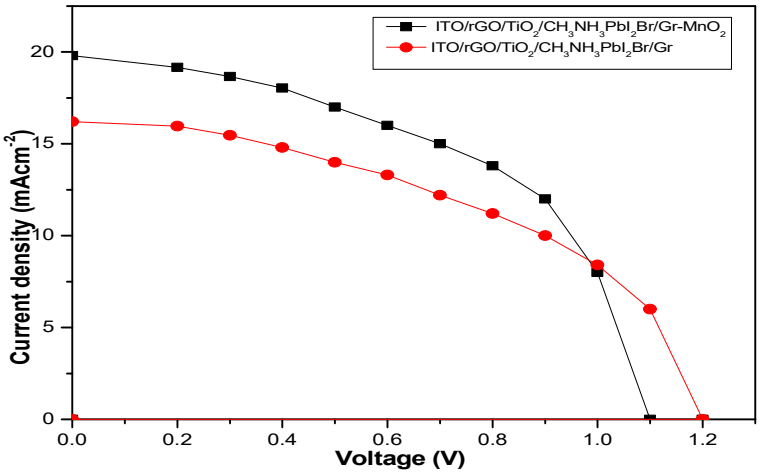

Figure 11. J-V curves of ITO/RGO/ TiO_2/$CH_3NH_3PbI_3$/Gr and ITO/RGO/ TiO_2/$CH_3NH_3PbI_3$/Gr-MnO_2 films

4. Conclusion

In this work, ITO/RGO/TiO_2/$CH_3NH_3PbI_3$/Gr and ITO/RGO/TiO_2/$CH_3NH_3PbI_3$/Gr-MnO_2 were fabricated on ITO glass slide using solution process-based spin coating method, and their properties were studied. The bandgaps of ITO/RGO/TiO_2/$CH_3NH_3PbI_3$/Gr-MnO_2 compared to ITO/RGO/TiO_2/$CH_3NH_3PbI_3$/Gr decreased from 1.75 to 1.65 eV. Besides, the XRD patterns showed variation in the intensity of diffraction angles. The average crystallite size and d-spacing of 657.37 nm and 5.797Å were calculated for ITO/RGO/TiO_2/$CH_3NH_3PbI_3$/Gr-MnO_2 compared to 576.05 nm and 5.956 Å calculated for ITO/RGO/TiO_2/$CH_3NH_3PbI_3$/Gr film. J-V curves of ITO/RGO/TiO_2/$CH_3NH_3PbI_3$/Gr and ITO/RGO/TiO_2/$CH_3NH_3PbI_3$/Gr-MnO_2 showed that the PCE

increased from 8.64% to 10.79%. The Jsc and FF also increased from 16.25 Acm^{-2}-19.00 Acm^{-2} and 47.48%-51.53% respectively. The enhancement value of 21.79% was achieved with MnO_2 passivation.

Acknowledgments: The authors profoundly acknowledge technical supports of the Material Science and Engineering Laboratory, KWASU, Molete and Industrial Laboratory, Pure and Applied Chemistry Department, LAUTECH, Ogbomoso.

Conflicts of Interest: The authors declare no conflicts of interest.

References

Awodugba A.O, Adedokun. O. (2011). On the physical and Optical Characterizationof CdS Thin Films Deposited by the Chemical Bath Deposition Technique, *The Pacific Journal of Sci. and Tech*, 334— 341

Bhatti H.S., HussainS.T., Khan F.A., Hussain S.(2016) Synthesis and induced multiferrroicity of perovskite $PbTiO_3$. *Appl. Surf. Sci.* 367:291-306

Chavan R.D., Prochovic D., BuczakB., Tavakoli M.M., Yedav P., Fialkowski M. and HongC.K. (2020) Gold Nanoparticle Functionalized with Fullerene Deivatives as an Effective Interface Layer for Improving the Efficiency and Stability of Planar Perovskite Solar Cells. *Adv. Mater.* Interface Early View 2001144

Chieng C.H., Nazeeruddin K., Gratzelc M. and Wu C.G. (2017) The Synergistic Effect On H_2O and DMF Towards Stable and 20 % Efficiency Inverted Perovskite Solar Cells. *Energy Environ. Sci.* 10, 808-817

Gao F., Zhang X., Zhao Y. and You J. (2019) Recent Progresses on Defect Passivation Towards Efficient Perovskite Solar Cells. *Adv. Energy Mater* 10, 1902650

Ihly R, Dowgiallo A M, Yang M, Schulz P, Stanton N J, Reid O G, Ferguson A J, Zhu K, Berry J J,Blackburn J L (2016). Efficient Charge Extraction and Slow Recombination in Organic– inorganic Perovskites Capped with Semiconducting Single walled Carbon Nanotubes. *Energy Environ. Sci.* 9, 1439-1449

Jiang J., Wang Q., Jin Z., Zhang X., Lei J., Bin H., Zhang Z., Li Y. and Liu S.F (2017)Polymer Doping for High-efficiency Perovskit eSolar Cell with Improved Moisture Stability. *Adv. Energy Mater* 8,1701757

Han T.H., Lee J.W., Choi C., Tan S., Lee C., Zhao Y., Dai Z., Marco N.D., Lee S.J., Bae S.H., Yuan Y.,Lee H.M., Huang Y., andYang Y.(2019) Perovskite Polymer Composite Cross-linker Approach for Highly Stable and Efficient Perovskite Solar Cells *Nat. Common.* 10, 520

Konios, D., et al., (2014) Dispersion behaviour of graphene oxide and reduced graphene oxide. *J Colloid Interface Sci*. 430: 108-12.

Markus D., Istiqomah I., Yusril A.F., Nasikhudin N., Yatimah A. and Worawat M. (2023) Potential of Enhancing MnO_2 based Composite and Numerous Morphological for Enhancing Supercapacitors Performance. *Journal of Material Sciences*. 20,2077-2098

Masclocene N., Guaghardi A.(2021) Coherent nanotwins and dynamic disorder in caecium lead halide perovskite nanocrystals *ACS Nano* 11,3819 3831

Mohamad, F.R, Hanifah, J. J., Madzlan, A., Ahmad, F. I, Mukhlis, A.R and Mohd., H. D (2015) Synthesis of Graphene Oxide Nanosheets via Modified Hummers' Method and Its Physicochemical Properties *Journal Teknologi (Sciences & Engineering) 74: 195–198*

Shao Y., Xiao Z.,Bi C., Yuan Y. and Huang J. (2014) Origin and Elimination of PhotocurrentHysteresis by Fullerene Passivation in $CH_3NH_3PbI_3$Planar Heterojunction Solar Cells *Nat Common* 5,5784

Subodh K (2006). *Spectroscopy of Organic Compounds*. Department of Chemistry, Guru Nanak Dev University Amritsar-143005

Suriyavathana, M. and Ramalingam, K. (2015) Nanoparticles Synthesis and Antibacterial Studyon Anisomeles Malabarica using Manganese Oxide (MnO), *International Journal of Chem. Tech Research*, Vol.8, No.11 pp 466-473.

Tumen-Ulzii G., Qui C., Leyden P., Wang P., Auffray M., Fujihara T., Matsushima T., Lee J.W,Lee S.J, Yang Y. and Aucachi C. (2020) Detrimental Effect of Unreacted PbI2 on the Long-term Stability of Pervskite Solar Cells *Adv. Mater* 1905035

Walton F., Wynne K. (2018) Control over phase separation and nucleation using a laser-tweezing potential. *Nat. Chem*. 10, 506-510

Wang Q., Dang Q., Li T., Gruverman A and Hasung J. (2024) Thin Insulating Tunneling Contact for Efficient and Water-resistant Perovskite Solar Cells *Adv Mater* 28,6734-6739

Yang S., Dai J., Yu Z., Zhou Y., Xiao X., Zeng X.C. and Huang J. (2019) TailoringPassivation Molecular Structures for Extremely Small Open-circuit Voltage Loss in Perovskite Solar Cells. *J. Am. Chem. Soc.* 141, 5781-5787